

Spatially resolved diagnostics of an atmospheric pressure direct current helium microplasma

Qiang Wang¹, Ivanka Koleva², Vincent M Donnelly¹ and Demetre J Economou¹

¹ Plasma Processing Laboratory, Department of Chemical Engineering, University of Houston, Houston, TX 77204-4004, USA

² Department of Physics, University of Sofia, Sofia BG-1164, Bulgaria

Received 17 January 2005

Published 20 May 2005

Online at stacks.iop.org/JPhysD/38/1690

Abstract

Optical emission spectroscopy measurements were performed with added trace probe gases in an atmospheric pressure direct current helium microplasma. Spatially resolved measurements (resolution $\sim 6 \mu\text{m}$) were taken across a $200 \mu\text{m}$ slot-type discharge. Gas temperature profiles were determined from N_2 emission rotational spectroscopy. Stark splitting of the hydrogen Balmer- β line was used to investigate the electric field distribution in the cathode sheath region. Electron densities were evaluated from the analysis of the spectral line broadening of H_β emission. The gas temperature was between 350 and 550 K, peaking nearer the cathode and increasing with power. The electron density in the bulk plasma was in the range $(4\text{--}7) \times 10^{13} \text{ cm}^{-3}$. The electric field peaked at the cathode ($\sim 60 \text{ kV cm}^{-1}$) and decayed to small values over a distance of $\sim 50 \mu\text{m}$ (sheath edge) from the cathode. These experimental data were generally in good agreement with a self-consistent one-dimensional model of the discharge.

1. Introduction

High pressure microplasma discharges (or microdischarges) have received considerable attention in recent years [1–13]. Such discharges are characterized by their small size (characteristic dimension $< 1 \text{ mm}$) and high gas pressure operation (100 Torr–1 atm). They are non-equilibrium glow discharges, with an electron temperature (tens of thousands of Kelvins) much higher than the gas temperature ($< 1000 \text{ K}$). Various designs of plasma sources to generate stable microplasma discharges have been proposed. The reported electrode configurations include parallel plates [7], cylindrical type (e.g. hollow cathode [1]), slot type [4], needle type [12] etc, and the applied operation modes vary from direct current (DC) to RF or microwave. Single microplasma sources can be integrated into arrays or matrix structures [3, 8]. These studies are motivated by numerous potential applications of microplasmas including sensors, integrated MEMS, excimer sources or microreactors [9–13].

The measurement of basic plasma characteristics, such as gas temperature, electron temperature, electron density,

electric field etc, is important for understanding discharge behaviour, and for extending the range of parameter space while maintaining stable discharge operation. Although extensive investigations of microdischarge modes and I – V characteristics have been reported, direct plasma diagnostics of microdischarges are still limited. The difficulties mostly arise from their small size and high operating pressure. Optical emission spectroscopy (OES) has proved to be a powerful technique in plasma diagnostics [14–17]. In this work, spatially resolved measurements of several plasma parameters of an atmospheric pressure DC helium microplasma are reported. Gas temperature, electron density and cathode sheath electric field were determined using OES of trace species (N_2 or H_2) added to the discharge. The experimental data were also used to validate a self-consistent discharge model.

2. Experimental

The slot-type microplasma source and electric circuit are sketched in figure 1. The source consisted of a 0.1 mm thick

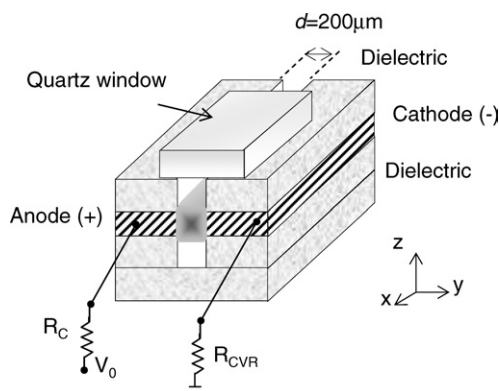


Figure 1. Slot-type DC microplasma source configuration and electrical circuit.

molybdenum foil, sandwiched between two dielectric layers (Al_2O_3 , each 0.15 mm thick). The base was also an alumina layer. The slot (0.2 mm wide, 0.4 mm deep and 6 mm long) was cut into the sandwich using a Buehler cutting tool with a diamond blade, forming a cell with parallel electrodes. To minimize the optical path-length and reduce self-absorption at high pressures, a quartz window was placed on top of the slot.

The microplasma source was inside a vacuum chamber so that a pure gas environment could be maintained and the discharge could be operated below atmospheric pressure. In this study, helium (99.999%) flowed at 2 slm. With the chamber evacuated and valved off, a leak rate of $0.3 \text{ mTorr min}^{-1}$ was measured, corresponding to an impurity level of 0.5 ppm in the He flow. Traces (0.02 mol%) of N_2 or H_2 were added to the He gas feed to measure the gas temperature (from N_2 rotational spectroscopy), electric field (from the H-Stark splitting effect) and electron density (from the H-Stark broadening effect). The pressure was 760 Torr in all experiments. A DC power supply with a ballast resistor ($R_C = 10 \text{ k}\Omega$ in figure 1) was used to generate a discharge in the confined channel geometry. The discharge voltage, V_d , was equal to the voltage difference between the two electrodes, and the discharge current, I_d , was derived from the voltage across a ‘current-view’ resistor ($R_{\text{CVR}} = 100 \Omega$ in figure 1). Figure 2 presents the I – V characteristic curves of the microplasma discharges used in this study (pure He, He/0.02% N_2 and He/0.02% H_2). All discharges operated in the abnormal glow mode, as indicated by the positive slope of the I – V characteristics. Hence, the current density was derived from the measured current divided by the electrode surface area.

Figure 3 shows a schematic diagram of the experimental set-up for OES measurements. The collection optics provided a $7\times$ magnification. Both objective and projection lenses were mounted on stages allowing precise translation of the lenses. The spectrometer consisted of a 0.55 m focal length monochromator (ISA TRIAX 550) with an 1800 lines mm^{-1} grating and a CCD detector (2000×800 pixels, $30 \text{ mm} \times 12 \text{ mm}$). The spectral resolution, determined using a low pressure Hg–Ar lamp, was 0.33 \AA with a $40 \mu\text{m}$ entrance slit width. Emission from the discharge, collected through a set of diaphragms and lenses, was focused onto the entrance slit of the monochromator. The entrance slit was parallel to the longitudinal direction (x -direction in figure 1) of the discharge

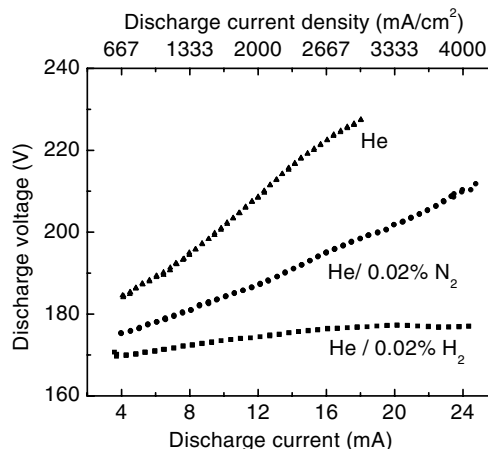


Figure 2. I – V characteristics of the microplasma discharge for the gases used in this study. (\blacktriangle —He, \bullet —He/0.02% N_2 , \blacksquare —He/0.02% H_2).

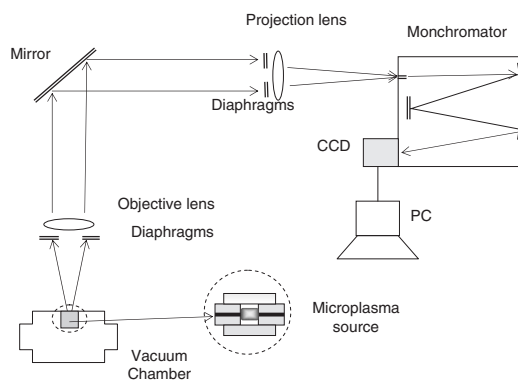


Figure 3. The schematic diagram of the experimental set-up for spatially resolved OES measurements.

image. The optical system provided a spatial resolution of about $6 \mu\text{m}$ across the $200 \mu\text{m}$ gap between the two electrodes (y -direction in figure 1). For the electric field measurements, a polarizing filter was placed between the two lenses.

A one-dimensional self-consistent fluid model of the He microplasma source was also developed. The governing equations included mass continuity for charged (e^- , He^+ and He_2^+) and neutral species (metastable states of He and He_2 , two radiation states of He), energy balances to determine the electron and gas temperatures, and Poisson’s equation for the electric field. The He plasma chemistry included reactions deemed to be important in high pressure discharges (Penning-ionization, dissociative recombination, collisional–radiative recombination, radiation trapping, etc). A detailed description of the model can be found in [18].

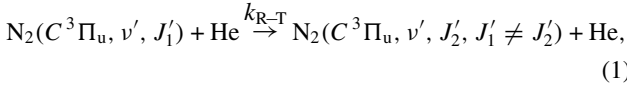
3. Results and discussion

3.1. Gas temperature measurements

The spatially resolved gas temperature was measured by adding a small amount (0.02 mol%) of N_2 to the He gas feed and recording N_2 ($C^3\Pi_u, v' = 0 \rightarrow B^3\Pi_g, v'' = 2$) emission in the ultraviolet region. This method has been widely used for low pressure ($<1 \text{ Torr}$) plasmas [17, 19–21]

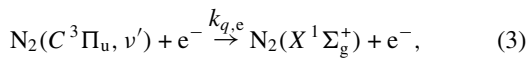
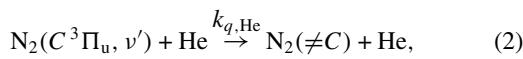
and in fewer cases for high pressure discharges, such as atmospheric plasma torches [22] and dielectric barrier discharges [23]. Except at very low pressures (species mean-free-path comparable to reactor dimensions), it may be assumed that the rotational population distribution of N_2 in its ground electronic state ($X^1\Sigma_g^+$), described by the rotational temperature, T_r , is equilibrated with the neutral gas temperature, T_g . Electron-impact excitation of ground state N_2 transfers its rotational population distribution ‘intact’ to the C-state [17]. If the time scales of other decay processes (see discussion below) are long compared to the radiative lifetime of the C-state, $\tau_{r,C} = 39$ ns [24], then T_r can be determined from the shape of the $C \rightarrow B$ rovibronic bands, provided that the rotational constants of the *ground state* of N_2 are used in the expression for the rotational population distribution. (The rotational constants for the C- and B-states are, of course, used to compute the wavelengths of the rovibronic emission bands.) This collision-free radiative decay of the $N_2(C^3\Pi_u)$ state occurs in low pressure discharges ($\lesssim 1$ Torr).

In high pressure plasmas, however, additional collisional processes occur. Under our experimental conditions, the fastest of these is likely to be rotational-to-translational (R–T) energy transfer between He and $N_2(C^3\Pi_u)$,



where k_{R-T} is the R–T rate constant of the C-state. It is expected that k_{R-T} for the C-state is of the same order as the reported state-to-state R–T rate constants of the ground state $N_2(\nu = 0)$ in He at room temperature ($k_{R-T} \sim 10^{-10}$ – 10^{-11} $\text{cm}^3 \text{s}^{-1}$ [25]). Hence, the time between R–T collisions, $\tau_{R-T} (= 1/k_{R-T} \cdot n_{He}) \ll \tau_{r,C}$ at atmospheric pressure, where n_{He} is the He number density.

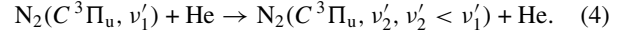
Electronic quenching of $N_2(C^3\Pi_u, \nu')$ by He or electrons can form N_2 in lower electronic states (quenching by N_2 itself can be ignored here due to the small N_2 addition)



where $k_{q,He} = 2 \times 10^{-12}$ $\text{cm}^3 \text{s}^{-1}$ ($\nu' = 0$) [26] and $k_{q,e} < 1 \times 10^{-9}$ $\text{cm}^3 \text{s}^{-1}$ ($\nu' = 0$) (estimated from detailed balance with the reported electron impact cross-section data in [27]) are the rate coefficients for electronic quenching of the $N_2(C^3\Pi_u, \nu')$ state by He and electrons, respectively. Since $n_e \sim 10^{14}$ cm^{-3} , quenching by electrons is much slower than radiative decay, as well as other collisional processes, and can therefore be ignored. The reported rate coefficient for electronic quenching by He should be regarded as the overall value because any dependence on the rotational level has not been investigated. If high J levels of $N_2(C^3\Pi_u, \nu')$ were electronically quenched near the R–T energy transfer rate (i.e. $k_{q,He}(\text{high } J) \sim k_{R-T}$), then the C-state rotational temperature would be lower than the gas temperature. If, on the other hand, $k_{q,He} \ll k_{R-T}$ for all observable J levels, any deviations from a thermalized rotational population of the C-state due to a J -dependence in electronic quenching, will be insignificant because of

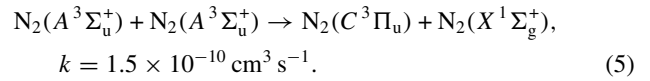
the much faster R–T energy transfer with He. Since the detailed J -dependent electronic quenching rate constants are expected to be of the same order of magnitude as the overall value of $\sim 2 \times 10^{-12}$ $\text{cm}^3 \text{s}^{-1}$, which is smaller than k_{R-T} , electronic quenching will only change the population, but not the population *distribution* of the C-state. Hence, electronic quenching will not affect the measured rotational temperature.

Vibrational quenching *within* the C-state can also occur



However, as long as $\nu'_1 = 0$ (as in this study), vibrational quenching is of no concern.

Other concerns may arise from the existence of alternate pathways to form the $N_2(C^3\Pi_u)$ state, besides electron impact excitation. For instance, $N_2(C^3\Pi_u)$ can be formed by metastable $N_2(A^3\Sigma_u^+)$ pooling reactions [23, 28]



This process was found to be the dominant production mechanism of the C-state in the afterglow of He/ N_2 plasmas in dielectric barrier discharges at atmospheric pressure [23]. In this case, the rotational energy partitioned into the $N_2(C^3\Pi_u)$ state may be dictated by the exothermicity of the pooling reaction, rather than the gas temperature. This would invalidate temperature measurements if the time scale of reaction (5) $\tau_5 < \tau_{R-T}$, but has no appreciable effect in this study, since $\tau_5 \gg \tau_{R-T}$ due to the relatively lower density of $N_2(A^3\Sigma_u^+)$ in comparison with He gas.

Radiation trapping of emission from the C-state due to absorption by the B-state may also affect the rotational population distribution [29]. Since lower J' levels, near the maximum in population ($J' = 8$ at 400 K), are present at higher concentrations and therefore absorb more light than high J' levels, the rotational temperature could appear to be significantly higher than the gas temperature. Under the present experimental conditions, this radiation trapping can be ruled out. The fraction of light absorbed, $(I_0 - I)/I_0 = 1 - 10^{-klp}$ can be estimated from the pathlength ($l = 0.025$ cm), the partial pressure, p (in Torr) of the $\nu'' = 2$ level of the $N_2(B^3\Sigma_g^-)$ state (conservatively estimated to be $< 0.1\%$ of the ground state N_2 number density, or $< 10^{-4}$ Torr) and the absorption coefficient, k , estimated to be ~ 100 $\text{cm}^{-1} \text{Torr}^{-1}$, using the procedure in [30], with the constants for N_2 C- and B-states. From this we estimate the maximum $(I_0 - I)/I_0$ to be $\sim 6 \times 10^{-4}$, i.e. much less than unity and, therefore, insignificant.

Consequently, at atmospheric pressure, the fast R–T energy exchange collisions between N_2 C-state and He dominate all other collisional processes and occur many times before N_2 emits; the N_2 C-state thermalizes with He, and the gas temperature can be determined directly from the C-state rotational temperature, provided that rotational population distributions are calculated with the rotational constants of the $N_2(C^3\Pi_u)$ state *and not the ground state*. (In fact, since the rotational constant B_{rot} for the ground state $N_2(X^1\Sigma_g^+)$ is nearly equal to that of the C-state, little error in temperature is made if the ground state constants are used.)

Finally, it should also be noted that under our experimental conditions, the transition $N_2(C^3\Pi_u, \nu' = 0 \rightarrow B^3\Pi_g, \nu'' = 2)$

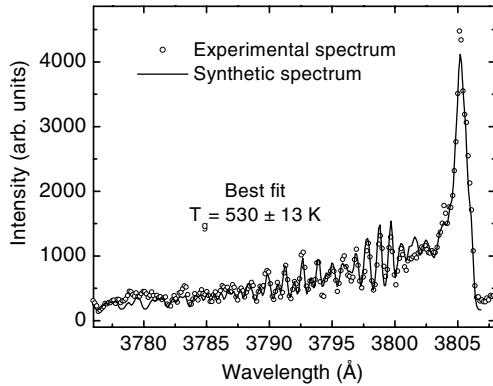


Figure 4. A sample of observed and synthetic spectra of the $N_2(C^3\Pi_u, v' = 0 \rightarrow B^3\Pi_g, v'' = 2)$ transition in He/0.02% N_2 DC microplasmas at $P = 760$ Torr. (Discharge condition: $I_d = 24$ mA, $V_d = 210$ V, at distance $d = 87$ μ m from cathode.)

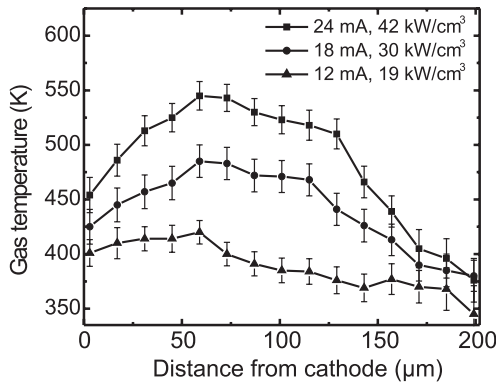


Figure 5. Gas temperatures in He/0.02% N_2 DC microplasmas at $P = 760$ Torr, determined from the $N_2(C^3\Pi_u, v' = 0 \rightarrow B^3\Pi_g, v'' = 2)$ transition as a function of position and power. (Discharge conditions of I_d , V_d , P_w and power density are: \blacksquare —24 mA, 210 V, 5.0 W, 42 kW cm^{-3} , \bullet —18 mA, 199 V, 3.6 W, 30 kW cm^{-3} and \blacktriangle —12 mA, 187 V, 2.3 W, 19 kW cm^{-3} .)

was found to be the best because of minimal interference with background emissions from He, He_2 and trace impurities such as H, OH, CO and CN.

Figure 4 shows an example of a comparison between the experimental and synthetic emission spectra of the $N_2(C^3\Pi_u, v' = 0 \rightarrow B^3\Pi_g, v'' = 2)$ transition. The gas temperature ($T_g = 530 \pm 13$ K) was obtained by matching the simulated rovibronic band with the observed spectrum and varying T_g to minimize χ^2 and achieve the best fit. (See [17] for the detailed fitting procedure.) Spatially resolved gas temperature measurements as a function of the discharge power are presented in figure 5. For each power, the gas temperature peaks closer to the cathode. The gas temperature increases with power, reaching about 550 K for the highest power examined. (This corresponds to a power density of about 42 kW cm^{-3} , estimated from the input power divided by the volume between the two electrodes.) Simulation results predicted the T_g distributions quite well (figure 6). The main gas heating mechanism in this high pressure He discharge was found to be ion Joule heating [18], i.e. energy transfer by collisions of ions with the background gas. In the cathode sheath region, the electric field is much higher than in the majority of the discharge (see electric field

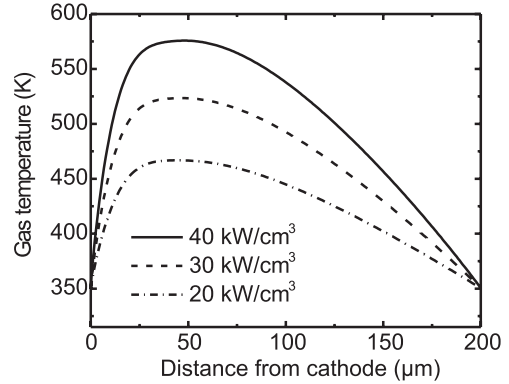


Figure 6. Simulation results of the gas temperature profile in He DC microplasmas at $P = 760$ Torr and at power density values similar to those in figure 5.

measurements in section 3.3). Positive ions gain energy from the field and collisionally transfer most of this energy to the neutral gas, thereby heating the gas, predominantly closer to the cathode. Direct comparison between measurements and simulation is difficult since the one-dimensional simulation is an over simplification of the plasma geometry. Also, the electrode surface temperature was not available. While both electrodes were assumed to be at 350 K in the simulation, it is expected that the cathode surface will be at a higher temperature than that of the anode (see figure 5).

Compared to conventional large scale plasma reactors used for microelectronics fabrication, the microplasma source has a much larger surface-to-volume ratio, facilitating heat loss through gas conduction to the boundaries. For He plasmas, heat loss is further enhanced due to the high thermal conductivity of the gas. Thus, despite the high power densities in the system, the measured maximum gas temperature was only about 550 K.

3.2. Electron density measurements

The spectral method for obtaining the electron density is based on the analysis of the wavelength profile of the 4861.3 \AA H_β line. A small amount of H_2 (0.02 mol%) was added into the He gas flow and the emission from the centre of the discharge was recorded. Compared to other hydrogen Balmer lines, the H_β line is often preferred because it has adequate emission intensity, higher sensitivity to electron density and lower susceptibility to self-absorption [31]. In the conditions of high pressure discharges, the H_β lineshape can be approximated with a Voigt function, resulting from a convolution of Gaussian and Lorentzian profiles. Gaussian profiles are a result of Doppler broadening and instrumental broadening, while Lorentzian profiles result from Stark broadening and Van der Waals broadening. (Resonance broadening can be ignored due to the small amount of H_2 addition.)

The full-width at half maximum (FWHM) of the Gaussian component of the Voigt profile, $\Delta\lambda_G$, is given by

$$\Delta\lambda_G = (\Delta\lambda_{\text{Doppler}}^2 + \Delta\lambda_{\text{Instrument}}^2)^{1/2}, \quad (6)$$

where $\Delta\lambda_{\text{Doppler}}$ and $\Delta\lambda_{\text{Instrument}}$ are the FWHM of Doppler and instrumental broadening, respectively.

Doppler broadening results from the movement of emitting atoms relative to the observer and yields a Gaussian profile, if the atomic velocities follow a Maxwellian distribution function. $\Delta\lambda_{\text{Doppler}}$ is given by the expression

$$\Delta\lambda_{\text{Doppler}} = 7.16 \times 10^{-7} \lambda \sqrt{\frac{T_h}{M}}, \quad (7)$$

where λ is the emission wavelength in \AA , T_h is the temperature of emitters in K (assumed to be equal to the gas temperature T_g) and M is the atomic weight of H atoms in g mol^{-1} . With the spectrometer entrance slit width set to $40 \mu\text{m}$, a value of 0.33\AA was observed for $\Delta\lambda_{\text{Instrument}}$.

The Lorentzian component of the Voigt profile, $\Delta\lambda_L$, is given by

$$\Delta\lambda_L = \Delta\lambda_{\text{Van der Waals}} + \Delta\lambda_{\text{Stark}}, \quad (8)$$

where $\Delta\lambda_{\text{Van der Waals}}$ and $\Delta\lambda_{\text{Stark}}$ are the FWHMs of Van der Waals and Stark broadening, respectively.

Van der Waals broadening is caused by collisions of excited H atoms (the emitters) with ground state He atoms (the perturbers). According to the general expression for Van der Waals broadening [32], the value of $\Delta\lambda_{\text{Van der Waals}}$ was estimated under our experimental conditions using the expression

$$\Delta\lambda_{\text{Van der Waals}} \approx 4.09 \times 10^{-13} \lambda^2 (\bar{\alpha} \bar{R}^2)^{2/5} \left(\frac{T_g}{\mu}\right)^{3/10} n_{\text{He}}, \quad (9)$$

where λ is the emission wavelength in \AA , $\bar{\alpha}$ is the average polarizability of neutral perturbers (i.e. He), given in cm^3 , and is equal to $1.38 \times a_0^3$ (a_0 is the Bohr radius in cm, and the value 1.38 is taken from [33]), the parameter $\bar{R}^2 \approx 600 \times a_0^2 \text{cm}^2$ is determined from the ionization energy of H and the upper and lower energy levels of the H_β , T_g is the gas temperature in K, $\mu = 0.8$ is the emitter–perturber reduced mass, and n_{He} is the neutral He gas density in cm^{-3} .

Stark broadening arises from the interaction between charged particles with excited H atoms, and its FWHM, $\Delta\lambda_{\text{Stark}}$, is given by [31]

$$\Delta\lambda_{\text{Stark}} = 2.5 \times 10^{-9} \alpha_{n'n} n_e^{2/3}, \quad (10)$$

where $\alpha_{n'n}$ is the tabulated parameter for each transition $n' - n$ and n_e is the electron density in cm^{-3} . To obtain electron density value in the range 10^{-13} – 10^{14}cm^{-3} , we used the $\alpha_{n'n}$ values in the table in [34] and the extrapolated values of tables in [31].

The recorded H_β spectral profile was normalized to its area and then fitted to a Voigt function according to the Maquardt–Levenberg method. $\Delta\lambda_G$, calculated from equation (6), was kept constant at a given gas temperature value. $\Delta\lambda_L$ was obtained from the best fit between the simulated Voigt profile and the experimental spectrum. Then, the Stark contribution, $\Delta\lambda_{\text{Stark}}$, was found from equation (8).

The electron density (at the centre of the discharge) as a function of discharge current is shown in figure 7. For these conditions, the FWHM values of various broadening components are listed in table 1. (T_g was taken from the gas temperature measurements presented earlier.) The measured electron density increases almost linearly with discharge current, from $4.0 \times 10^{13} \text{cm}^{-3}$ at 8 mA to $7.3 \times 10^{13} \text{cm}^{-3}$

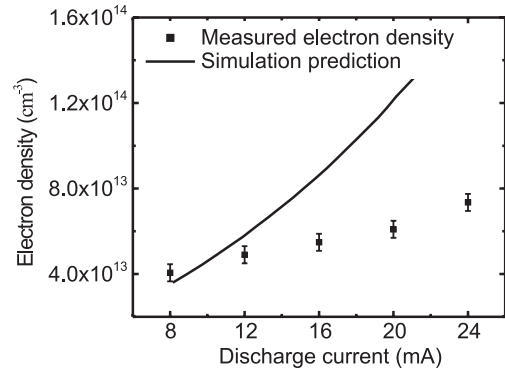


Figure 7. Bulk electron densities in He/0.02% H_2 DC microplasmas at $P = 760$ Torr as a function of current. The figure also shows the simulation prediction of electron densities at the same current values.

Table 1. FWHM of instrumental, Doppler, Van der Waals and Stark broadening (\AA) for H_β spectral profiles at different discharge currents (T_g is the gas temperature).

I_d (mA)	T_g (K)	$\Delta\lambda_{\text{Instrument}}$	$\Delta\lambda_{\text{Doppler}}$	$\Delta\lambda_{\text{Van der Waals}}$	$\Delta\lambda_{\text{Stark}}$
8.0	320	0.33	0.062	0.51	0.21
12.0	370	0.33	0.067	0.47	0.24
16.0	420	0.33	0.071	0.44	0.26
20.0	470	0.33	0.075	0.42	0.28
24.0	520	0.33	0.079	0.38	0.32

at 24 mA. Under the present experimental conditions of atmospheric pressure, gas temperature < 600 K, and electron density $< 10^{14} \text{cm}^{-3}$, Van der Waals broadening was equal to or larger than Stark broadening, causing the error of this analysis to mostly depend on the accuracy of the gas temperature. It should be noted that electron density measurements were taken only in the field free bulk plasma to avoid electric field contributions to the broadening of the lineshape, which would greatly complicate the extraction of the electron density [35]. The predicted electron density as a function of the discharge current changes is also presented in figure 7. Simulation shows a similar trend of electron density with discharge current, albeit the electron densities were higher [18]. This discrepancy can again be due to the fact that the simulation was one-dimensional while the discharge system is two-dimensional.

3.3. Electric field measurements

Polarization-dependent Stark spectra of the hydrogen Balmer series (H_α , H_β , H_δ etc) have been used to measure the electric field distribution in the sheath region of low pressure discharges [36–39]. The technique is based on the Stark effect, in which the fine energy levels of hydrogen atoms split in the presence of an electric field, and consequently the components of the hydrogen Balmer emission shift from the line centre [40]. In this work, a small amount of hydrogen (0.02 mol%) is added to the He gas, and emission from H_β lines is recorded through a polarizer. With the polarizer axis set along the x -direction in figure 1 (perpendicular to the direction of the electric field), only emission of the σ components ($\Delta m = \pm 1$, where m is the magnetic quantum number) of the H_β line was allowed to pass through the polarizer, while its π components ($\Delta m = 0$)

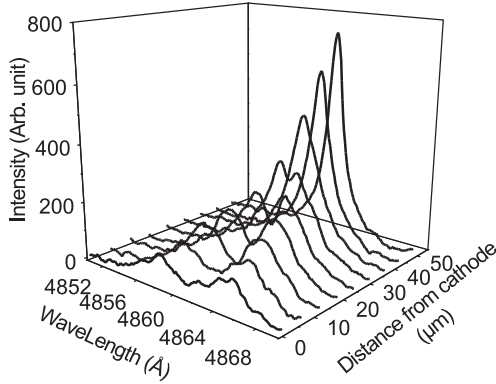


Figure 8. Observed spectra of H_{β} (σ components) emission in the cathode sheath of He/0.02% H_2 DC microplasmas at $P = 760$ Torr. (Discharge condition: $I_d = 24.1$ mA, $V_d = 177$ V.)

were selected to transmit, with the polarizer axis parallel to the electric field.

The observed emission profiles of H_{β} (σ components) as a function of position in the cathode sheath region are shown in figure 8. The most broadened profile with two peaks is located nearest to the cathode surface, indicating the highest electric field in this region. The peak splitting decreases with distance away from the cathode and the two peaks eventually merge into one, indicating a monotonically decreasing electric field.

To determine the electric field strength quantitatively, a fitting procedure was developed. At high pressure, the emission profile of each Stark component (σ or π) of the H_{β} line is expected to have a Voigt function. In the model, the Voigt function (V) was approximated by the sum of a Gaussian (G) and a Lorentzian (L) function, according to [41]:

$$V(\lambda) = (1 - \eta)G(\lambda) + \eta L(\lambda), \quad (11)$$

where λ is the emission wavelength. $\Delta\lambda_V$, the FWHM of the Voigt function, was estimated from the FWHMs of Gaussian and Lorentzian profiles as [41]

$$\Delta\lambda_V \approx \frac{\Delta\lambda_L}{2} + \sqrt{\frac{\Delta\lambda_L^2}{4} + \Delta\lambda_G^2}, \quad (12)$$

where $\Delta\lambda_G$ and $\Delta\lambda_L$ were calculated using equations (6) and (8), respectively. Under our experimental conditions, a Gaussian type function is mainly attributed to instrumental broadening, because $\Delta\lambda_{\text{Doppler}}^2 \ll \Delta\lambda_{\text{Instrument}}^2$ in equation (6). On the other hand, because the electron density is expected to be relatively small in the sheath region, the corresponding Stark width can be ignored compared to the Van der Waals width. Thus, equation (8) simplifies to $\Delta\lambda_L \approx \Delta\lambda_{\text{Van der Waals}}$.

It should be mentioned that in low pressure discharges, the Doppler effect, due to fast H atoms created by charge exchange of ions accelerated in the sheath, or by ions backscattered from the electrode, was usually taken into account to simulate the lineshape of each Stark component in the cathode sheath region where ion energies can reach hundreds of electron volts [36–39], but it should be negligible at high pressures due to the high collision rate of the ions.

The parameter η in equation (11) determining the fraction of the Lorentzian part is given by

$$\eta = \frac{\Delta\lambda_L / \Delta\lambda_V}{\Delta\lambda_L / \Delta\lambda_V + (\Delta\lambda_G / \Delta\lambda_V)^2}. \quad (13)$$

The normalized Gaussian (G) and Lorentzian (L) functions are given by the expressions [41]

$$G(\lambda) = \exp\left(-4 \times \ln 2 \left(\frac{\lambda - \lambda_0}{\Delta\lambda_V}\right)^2\right), \quad (14)$$

$$L(\lambda) = \frac{1}{1 + 4 \times ((\lambda - \lambda_0) / \Delta\lambda_V)^2}, \quad (15)$$

where λ_0 is the centre wavelength of H_{β} .

In the presence of an electric field of magnitude E , each Stark component is shifted from the centre of the spectral transition, and the shifted wavelength, $\Delta\lambda_k$, is given by [40]

$$\Delta\lambda_k(k, E) = 1.517 \times 10^{-2} k \cdot E, \quad (16)$$

where $\Delta\lambda_k$ is in \AA , E is in kV cm^{-1} and k is the Stark component number of the H_{β} line (e.g. $k = \pm 2, \pm 4, \pm 6, \pm 10, \pm 12$ for its σ components [40]). Equation (16) indicates that the splitting of each component is proportional to the electric field strength.

For a given value of E , the H_{β} profile was the superposition of all broadened Stark components. By combining equations (11) and (16), we have

$$I(\lambda, E) = \sum_k I_k \cdot V(\lambda - \Delta\lambda_k(k, E)), \quad (17)$$

where I_k is the relative peak height of each broadened Stark component, derived from the reported relative intensity [40].

Finally, the presence of electric field gradients in the volume over which emission was sampled was also taken into account by summing the synthetic spectra over a range of electric field strengths ($E - \Delta E$) to ($E + \Delta E$). The relative intensity for different electric fields was weighted equally. The final synthetic spectrum was given by

$$\begin{aligned} I_{\text{sum}}(\lambda, E, \Delta E) &= \sum_{E'=E-\Delta E}^{E'=E+\Delta E} I(\lambda, E') \\ &= \sum_{E'=E-\Delta E}^{E'=E+\Delta E} \sum_k I_k \cdot V(\lambda - \Delta\lambda_k(k, E')). \end{aligned} \quad (18)$$

The obtained synthetic profile was compared with the experimental spectrum (with intensities normalized), and the electric field strength was deduced from the best fit by changing the fitting parameters E and ΔE .

Examples of the fitting of synthetic H_{β} (σ components) profiles to observed profiles for both high and low electric field strength cases are shown in figure 9. Good agreement between experimental and calculated profiles is observed. The fitting procedure applied allowed us to determine electric field strengths as small as 1 kV cm^{-1} .

The measured electric field strength as a function of position in the cathode sheath region is shown in figure 10. The electric field peaks at the cathode surface and decreases monotonically to very small values in the bulk plasma.

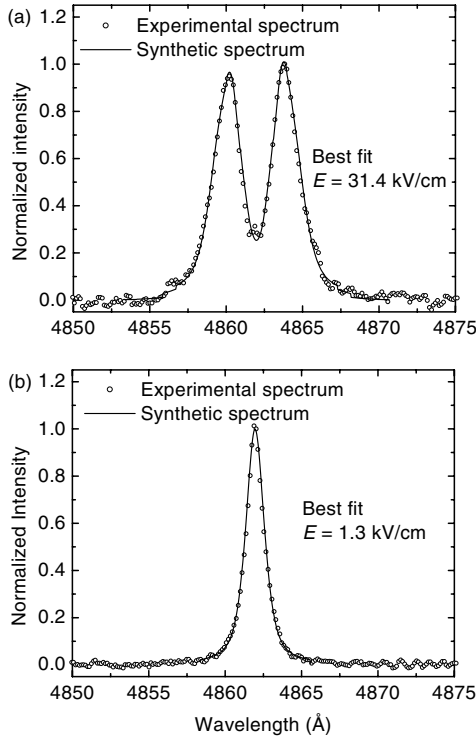


Figure 9. Samples of observed and synthetic spectra of H_{β} (σ components) lines in He/0.02% H_2 DC microplasmas at $P = 760$ Torr. (Discharge conditions: $I_d = 24.1$ mA, $V_d = 177$ V, at a distance $d = 24 \mu\text{m}$ (a) and $d = 48 \mu\text{m}$ (b) from the cathode.)

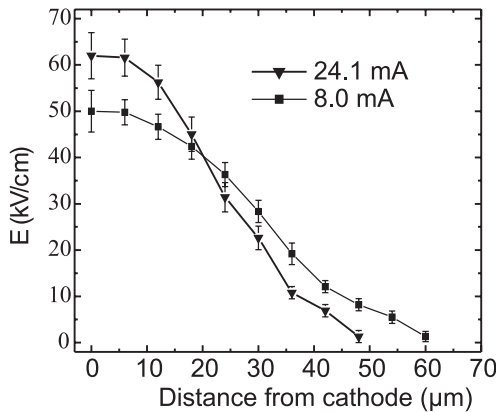


Figure 10. Electric field strength in the cathode sheath region in He/0.02% H_2 DC microplasmas as a function of current at $P = 760$ Torr. (Discharge conditions: \blacktriangledown — $I_d = 24.1$ mA, $V_d = 177$ V, \blacksquare — $I_d = 8.0$ mA, $V_d = 172$ V.)

The cathode sheath thickness (found by extrapolation) is between 50 and 60 μm for the two discharge currents shown. The sheath becomes wider as the discharge current decreases with a concomitant decrease in electron density. Integration of the electric field over the cathode sheath gives a sheath voltage drop of 164 V for 8 mA and 160 V for 24 mA, within 10% of the applied voltage.

Simulation results of the electric field distribution in the cathode sheath captured the trend found in the measurements, but the simulation predicted higher electric fields (see figure 11). This was probably because the simulation was

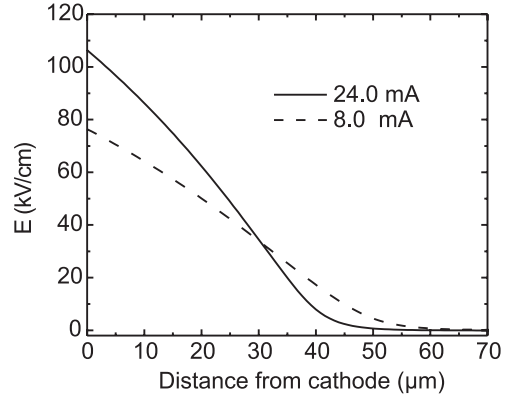


Figure 11. Simulation results of electric field strength in the cathode sheath region in He DC microplasmas at $P = 760$ Torr and at the same current values as in figure 10.

for pure helium and, for the same current, the discharge voltage was found to be considerably higher even when 0.02% of a molecular gas (in this case hydrogen) was added to the plasma (see figure 2). Nevertheless, a wider sheath was predicted at lower currents just as found experimentally, and the simulated sheath thickness was quite similar to the measured values.

4. Conclusions

OES from trace amounts (0.02%) of N_2 or H_2 was employed to characterize a slot-type DC atmospheric pressure He microplasma source. The gas temperature was determined by N_2 rotational spectroscopy, while Balmer H_{β} emission was used to determine the electric field distribution (from the Stark splitting effect) and electron density (from the Stark broadening effect). The measured gas temperature was between 350 and 550 K, peaking nearer the cathode and increasing with power. The electron density in the bulk plasma was in the range $(4-7) \times 10^{13} \text{ cm}^{-3}$. The measured electric field peaked at the cathode and decayed to small values over a distance of $\sim 50 \mu\text{m}$ (sheath edge) from the cathode. Several issues involved in performing gas temperature measurements by nitrogen rotational spectroscopy in high pressure discharges were discussed. Finally, the experimental measurements were generally in good agreement with the results of a one-dimensional simulation of the discharge. Detailed simulation results will be presented in [18].

Acknowledgments

The authors would like to thank the Department of Energy (Grant no. DE-FG02-03ER54713) and the National Science Foundation (CTS-0072854) for funding support. VMD would also like to thank Agere Systems and Bell Laboratories for equipment donations. IK is grateful to the Fulbright Foundation for financial support.

References

[1] Schoenbach K H, El-Habachi A, Shi W and Ciocca M 1997 *Plasma Sources Sci. Technol.* **6** 468

- [2] Stark R H and Schoenbach K H 1999 *Appl. Phys. Lett.* **74** 3770
- [3] Schoenbach K H, Moselhy M, Shi W and Bentley R 2003 *J. Vac. Sci. Technol. A* **21** 1260
- [4] Yu Z, Hoshimiya K, Williams J D, Polvinen S F and Collins G J 2003 *Appl. Phys. Lett.* **83** 854
- [5] Park S-J and Eden J G 2002 *Appl. Phys. Lett.* **81** 4127
- [6] Hsu D D and Graves D B 2003 *J. Phys. D: Appl. Phys.* **36** 2898
- [7] Yoshiki H and Horiike Y 2001 *Japan. J. Appl. Phys.* **40** (part 2) L360
- [8] Taniguchi K, Fukasawa T, Yoshiki H and Horiike Y 2003 *Japan. J. Appl. Phys.* **42** 6584
- [9] Eijkel J C T, Stoeri H and Manz A 2000 *Anal. Chem.* **72** 2547
- [10] Iza F and Hopwood J A 2003 *IEEE Trans. Plasma Sci.* **31** 782
- [11] Moselhy M, Shi W, Stark R H and Schoenbach K H 2002 *IEEE Trans. Plasma Sci.* **30** 198
- [12] Kikuchi T, Hasegawa Y and Shirai H 2004 *J. Phys. D: Appl. Phys.* **37** 1537
- [13] Qiu H, Martus K, Lee W Y and Becker K 2004 *Int. J. Mass Spectrom.* **233** 19
- [14] Malyshev M V and Donnelly V M 2001 *J. Appl. Phys.* **90** 1130
- [15] Malyshev M V and Donnelly V M 2001 *Phys. Rev. E* **60** 6016
- [16] Malyshev M V and Donnelly V M 1997 *J. Vac. Sci. Technol. A* **15** 550
- [17] Donnelly V M and Malyshev M V 2000 *Appl. Phys. Lett.* **77** 2467
- [18] Wang Q, Economou D J and Donnelly V M unpublished
- [19] Davis G P and Gottscho R A 1979 *J. Appl. Phys.* **54** 3080
- [20] Schabel M J, Donnelly V M, Kornblit A and Tai W W 2002 *J. Vac. Sci. Technol. A* **20** 555
- [21] Tonnis E J and Graves D B 2002 *J. Vac. Sci. Technol. A* **20** 1787
- [22] Laux C O, Spence T G, Kruger C H and Zare R N 2003 *Plasma Sources Sci. Technol.* **12** 125
- [23] Bibinov N K, Fateev A A and Wiesemann K 2001 *J. Phys. D: Appl. Phys.* **34** 1819
- [24] Johnso A W and Fowler R G 1970 *J. Chem. Phys.* **53** 65
- [25] Mate B, Thibault F, Ramos A, Tejada G, Fernandez J M and Montero S 2003 *J. Chem. Phys.* **118** 4477
- [26] Gat E, Gherardi N, Lemoing S, Massines F and Ricard A 1999 *Chem. Phys. Lett.* **306** 263
- [27] Simek M 2002 *J. Phys. D: Appl. Phys.* **35** 1967
- [28] Benedictis S D and Dilecce G 1995 *Plasma Source Sci. Technol.* **4** 212
- [29] Phillips D M 1975 *J. Phys. D: Appl. Phys.* **8** 507
- [30] Donnelly V M, Flamm D L and Collins G 1982 *J. Vac. Sci. Technol.* **21** 817
- [31] Luque J M, Calzada M D and Sáez M 2003 *J. Phys. B: At. Mol. Opt. Phys.* **36** 1573
- [32] Drake G W F (ed) 1996 *Atomic, Molecular and Optical Physics Handbook* (New York: American Institute of Physics) p 151
- [33] Mitroy J and Bromley M W 2003 *Phys. Rev. A* **68** 5201
- [34] Gigosos M A and Cardenoso V 1996 *J. Phys. B: At. Mol. Opt. Phys.* **29** 4795
- [35] Olchawa W, Olchawa R and Grabowski B 2004 *Eur. Phys. J. D* **28** 119
- [36] Barbeau C and Jolly J 1991 *Appl. Phys. Lett.* **58** 237
- [37] Booth J, Derouard J, Fadlallah M and Sadeghi N 1993 *J. Appl. Phys.* **74** 862
- [38] Wujec T, Janus H W and Jeleński W 2003 *J. Phys. D: Appl. Phys.* **36** 868
- [39] Barbeau C and Jolly J 1990 *J. Phys. D: Appl. Phys.* **23** 1168
- [40] Ryde N 1976 *Atoms and Molecules in Electric Fields* (Stockholm: Almquist) chapter 4
- [41] Payling R, Jones D and Bengtson A (ed) 1997 *Glow Discharge Optical Emission Spectrometry* (New York: Wiley) chapter 8.5